

SpecGen: Neural Spectral BRDF Generation via Spectral-Spatial Tri-plane Aggregation

Zhenyu Jin, Wenjie Li, Zhanyu Ma, and Heng Guo

Abstract—Synthesizing spectral images across different wavelengths is essential for photorealistic rendering. Unlike conventional spectral uplifting methods that convert RGB images into spectral ones, we introduce SpecGen, a novel method that generates spectral bidirectional reflectance distribution functions (BRDFs) from a single RGB image of a sphere. This enables spectral image rendering under arbitrary illuminations and shapes covered by the corresponding material. A key challenge in spectral BRDF generation is the scarcity of measured spectral BRDF data. To address this, we propose the Spectral-Spatial Tri-plane Aggregation (SSTA) network, which models reflectance responses across wavelengths and incident-outgoing directions, allowing the training strategy to leverage abundant RGB BRDF data to enhance spectral BRDF generation. Experiments show that our method accurately reconstructs spectral BRDFs from limited spectral data and surpasses state-of-the-art methods in hyperspectral image reconstruction, achieving an improvement of 8 dB in PSNR. Codes and data will be released upon acceptance.

I. INTRODUCTION

Real light is composed of a spectrum of wavelengths, and photorealistic image synthesis requires capturing the wavelength-dependent reflectance properties of materials under varying illumination and viewing conditions. Spectral bidirectional reflectance distribution functions (BRDFs) constitute a crucial ingredient in this process, enabling the synthesis of hyperspectral images for remote sensing [1], [2], material analysis [3], and virtual reality [4], as well as for classification tasks [5]. However, acquiring high-quality spectral BRDF data is challenging, as the measurement process requires scanning a four-dimensional domain at high resolution—a tedious and time-consuming task [6], leading existing spectral BRDF datasets to be scarce and limited in scale. To bypass the need for extensive spectral measurements, it is desired to develop a spectral BRDF generation method that can produce photorealistic spectral BRDFs from a single image input.

Existing methods have attempted to address BRDF generation, but they primarily focus on RGB BRDFs. For example, Gokbudak *et al.* [7] proposes a hypernetwork to reconstruct measured RGB BRDF from sparse samples. ControlMat [8] and MatFuse [9] leverage diffusion models to generate spatially-varying BRDFs, including albedo, roughness, metallic, and normal maps, from a single flash RGB photo. These methods, though effective in RGB BRDF generation, cannot be directly extended to spectral BRDFs due to differences in BRDF representation and the lack of spectral BRDF data. On the other

hand, another line of research explores spectral uplifting [10]–[13], which generates spectral images from RGB inputs. These methods mainly focus on producing spectral images, making extracting the underlying spectral BRDFs from the RGB inputs challenging. As a result, they cannot transfer the appearance of spectral material to different shapes and illuminations, a capability that is crucial for downstream image editing tasks. In summary, despite significant progress in spectral image generation and RGB BRDF generation, spectral BRDF generation remains an open problem.

The key challenge of spectral BRDF generation lies in the scarcity of spectral BRDF data. Currently, only 51 isotropic spectral BRDFs are publicly available [6], which makes it difficult to train high-quality, generalizable models. In contrast, measured RGB BRDF datasets, such as MERL [14], are relatively easy to collect and are available at a much larger scale. Our key insight is to design a compatible spectral BRDF representation, along with a training strategy that leverages large-scale RGB BRDF data to facilitate spectral BRDF generation.

In this paper, we propose SpecGen, which, to the best of our knowledge, is the first network to generate spectral BRDFs from a single RGB image. The core of SpecGen is the Spectral-Spatial Tri-plane Aggregation (SSTA) module, which facilitates the mapping between RGB and spectral BRDFs. Specifically, spectral BRDFs can be represented as a 4D function of $(\theta_h, \theta_d, \varphi_d, \lambda)$, where the spatial attributes $(\theta_h, \theta_d, \varphi_d)$ —related to incident and outgoing directions—are shared between spectral and RGB BRDFs, while the spectral attribute λ (wavelength) is unique to spectral BRDFs. Inspired by the 4D function decomposition in dynamic neural radiance fields (x, y, z, t) , we decompose the spatial and spectral attributes into two tri-planes, encoding their corresponding latent features separately. Building upon this tri-plane representation, we design a training strategy that leverages large-scale RGB BRDF datasets to supervise the spatial tri-planes, thereby alleviating the data scarcity issue in the spectral domain. Furthermore, to effectively integrate RGB and spectral features, we propose an Adaptive Feature Fusion (AFF) module, which replaces traditional feature fusion methods such as the Hadamard product [15]. The AFF module enhances the model’s representational capability by adaptively combining multi-plane features. As shown in Fig. 1, these dedicated designs enable our method to accurately generate spectral BRDFs and to facilitate downstream spectral rendering tasks.

To summarize, our main contributions are as follows:

- SpecGen is, to the best of our knowledge, the first spectral BRDF generation framework capable of generating

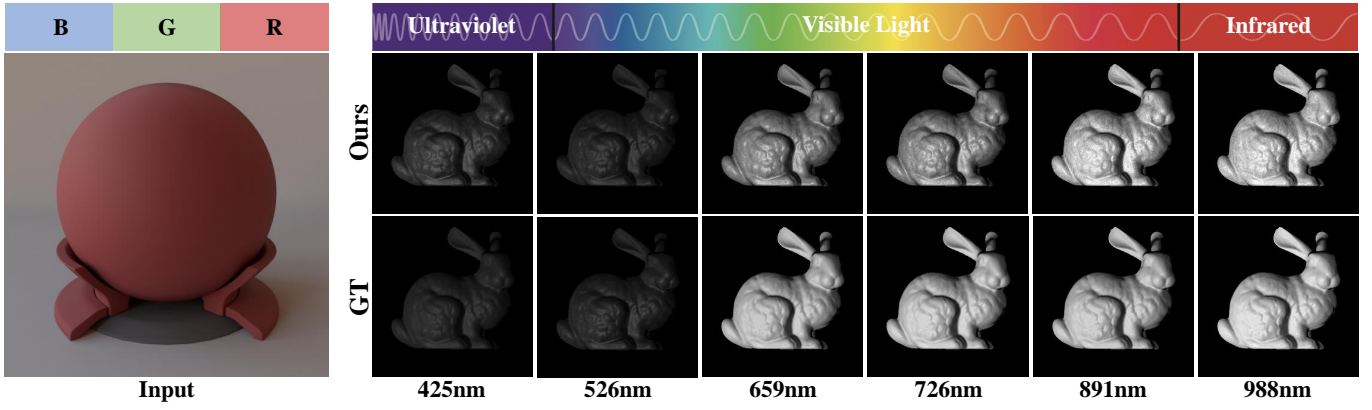


Figure 1: From a single RGB image of a sphere (left), our method recovers the spectral BRDF of the corresponding material, allowing the spectral image rendering of arbitrary illuminations and shapes covered by the material under different wavelengths (right). See Fig. 5 for more spectral renderings at more diverse wavelengths.

photorealistic spectral BRDFs from a single RGB image.

- We introduce the SSTA module, which alleviates the scarcity of spectral BRDF data by leveraging large-scale RGB BRDF datasets through a novel tri-plane representation of spectral and spatial BRDF attributes.
- We present the AFF module, which dynamically selects and fuses RGB and spectral features to enhance the model’s representational capacity.

Extensive experiments demonstrate that our method can reconstruct and generate high-quality spectral BRDFs, benefiting downstream tasks such as hyperspectral image rendering.

II. RELATED WORK

As shown in Table I, we summarize existing methods for BRDF generation and spectral image reconstruction from RGB images. Since our method is based on neural implicit representations, we also briefly review relevant works on spectral BRDF generation and neural implicit representations.

A. BRDF Generation

BRDF reconstruction and generation play a key role in advancing computer graphics and material analysis. Early methods, such as those based on CNNs [16], [17], extract spatially varying BRDFs (SVBRDFs) from images, but struggle with generalization and require separate training for each material. Later works utilize U-Net architectures [18], [19], which improve generalization performance but often fail to preserve fine details, particularly in highlight regions. To address this limitation, GAN-based methods [20]–[22] have gained popularity. For instance, SurfaceNet [20] and MaterialGAN [21] utilize GAN structures to generate realistic SVBRDFs from a single image. TileGen [22] extends MaterialGAN by training category-specific models, while PhotoMat [23] builds upon prior works by incorporating real-world datasets to further enhance visual quality.

With the rise of diffusion models [24], recent work has explored diffusion-based approaches for BRDF generation, such as ControlMat [8] and MatFuse [9]. These methods address the

low-quality artifacts observed in GAN-based approaches, but suffer from slower generation speeds. To improve inference efficiency, meta-learning-based methods [25], [26] have been proposed, achieving faster generation at the cost of reduced accuracy. Whereas all aforementioned methods focus solely on RGB BRDF generation, our approach, to the best of our knowledge, is the first to enable both RGB and spectral BRDF representation and generation.

The above BRDF generation methods are based on parametric reflectance models [27], representing reflectance via parameters such as albedo, roughness, and metallicity. Another line of research focuses on measured BRDFs, such as the MERL [14] and RGL [6] datasets. Matusik *et al.* [14] propose a data-driven BRDF generation model using PCA basis extraction. Gokbudak *et al.* [7] introduce a continuous neural BRDF representation for sparse reconstruction of BRDFs for unseen materials. Narumoto *et al.* [28] propose a neural embedding for BRDFs and a temporal model to represent BRDF changes in latent space. However, these methods primarily focus on RGB BRDFs, leaving the problem of spectral BRDF generation largely unexplored.

B. Implicit Neural Representations

Unlike traditional discrete representations—such as meshes, voxels, or point grids—which store sampled values at fixed locations, incurring substantial memory costs, suffering from aliasing, and requiring explicit interpolation schemes to achieve smoothness [29]—implicit neural representations (INRs) employ a learnable function (typically an MLP) that directly maps each continuous coordinate in the signal domain to its corresponding signal value. This formulation endows INRs with several attractive properties: they are resolution-independent, differentiable, and drastically more memory-efficient than high-resolution grids. A growing body of work validates these advantages across diverse domains. For example, SIREN [30] uses sinusoidal activations to capture high-frequency natural signals and their derivatives; NeRF [31] represents static scenes as continuous 5-D radiance fields for photorealistic novel-view synthesis; Neural Descriptor Fields (NDFs) [32]

Table I: Summary of existing representative methods on BRDF generation.

Method	Input	Output	Main Technology	Generate spectral BRDF
ControlMat [8], MatFuse [9]	RGB Image	RGB SVBRDF	Diffusion Model	×
PhotoMat [23], TileGen [22]	Flash RGB Image	RGB SVBRDF	GAN	×
Metappearance [25]	Image & Light	RGB BRDF	Meta Learning	×
Gokbudak <i>et al.</i> [7]	BRDF Sampling Data	RGB BRDF	Hyper Network	×
Narumoto <i>et al.</i> [28]	BRDF Sampling Data	Time-varying RGB BRDF	Coordinate-based MLP	×
Ours	Image	(RGB+Spectral) BRDF	Triplane Representation	✓

encode object points along with their relative poses, enabling smooth interpolation of robot grasp trajectories; and Local Implicit Neural Representation (LINR) [33] modules enhance fine-grained visual tracking by refining target regions with coordinate-based implicit functions.

Building on this foundation, K-Planes [15] replaces the monolithic MLP with a set of locally parameterized feature planes, thereby reducing the memory requirement from $O(N^4)$ to $O(6N^2)$ for four-dimensional signals and enabling asymmetric supervision across coordinate subsets. Inspired by K-Planes, our SpecGen introduces a novel spectral and spatial triplane representation to effectively decompose and model spectral BRDFs, thereby addressing the challenge of data scarcity in spectral BRDF generation.

C. Hyperspectral Image Reconstruction

Hyperspectral image (HSI) reconstruction aims to recover a full spectral data cube—comprising two spatial dimensions and one spectral dimension—from inputs with limited spectral resolution, such as RGB photos. Li *et al.* [10] show that deep CNNs can enhance textures and synthesize plausible spectra. Wang *et al.* [11] further improve robustness by framing the task as an optimization problem and adopting data-driven priors. More recently, Cai *et al.* [34] employ a mask-guided spectral transformer with self-attention to capture long-range spatial-spectral relationships, achieving state-of-the-art results.

Despite these advances, existing HSI methods operate strictly in the image domain: they “uplift” the per-pixel spectral signatures of the input frame but cannot disentangle the underlying material reflectance from lighting and geometry. Consequently, the recovered spectra cannot be transferred to new shapes, viewing directions, or illumination environments, limiting their usefulness in downstream graphics and vision tasks such as relighting, compositing, or physically based simulation. In contrast, our spectral-BRDF generation paradigm explicitly models the bidirectional and wavelength-dependent reflectance of the material itself, enabling faithful spectral rendering on arbitrary geometries and under arbitrary lighting.

III. METHOD

As shown in Fig. 2, given an input RGB image, the SSTA network leverages an encoder-decoder to extract two sets of triplanes: a spatial triplane that encodes the reflectance response of incident and outgoing light angles, and a spectral triplane that captures the reflectance responses jointly across angles and wavelengths. Next, we project wavelengths and incident-outgoing angles, represented in Rusinkiewicz coordinates [35],

onto the two triplanes to generate six feature vectors. The AFF module then fuses these features and produces a latent BRDF feature, which is used as input for our MLP-based BRDF mapping module to predict the corresponding spectral reflectance r .

A. Spectral-Spatial Tri-plane Aggregation

a) *Insight: K-Planes [15] for Dynamic Neural Radiance Field.*: Dynamic neural radiance fields can be represented as a 4D function with respect to 3D spatial location (x, y, z) and a 1D timestamp t . Therefore, K-Planes [15], as a dynamic NeRF method, models the dynamic scene radiance c as

$$c = f(x, y, z, t). \quad (1)$$

To decompose the static canonical scene and dynamic motion field, K-Planes [15] introduces a planar factorization that represents this 4D function using C_4^2 feature planes. Among these, three planes $\{(x, y), (x, z), (y, z)\}$ encode spatial domain information, while the remaining three $\{(x, t), (y, t), (z, t)\}$ capture spatial-temporal variations, thus enabling a clear decoupling of the static radiance field and temporal motion field.

b) *Spectral BRDF Representation*: Based on Rusinkiewicz coordinates [35], the spectral BRDF response can also be modeled as a 4D function of the incident-outgoing angles $(\theta_h, \theta_d, \varphi_d)$ and wavelength λ . Specifically, given incident and outgoing light directions ω_i and ω_o , the half vector can be calculated as $\mathbf{h} = \frac{\omega_i + \omega_o}{\|\omega_i + \omega_o\|}$. The angle θ_h denotes the polar angle of \mathbf{h} relative to the fixed surface normal $\mathbf{n} = (0, 0, 1)$; θ_d is the polar angle between the outgoing direction ω_o and the half-vector \mathbf{h} ; φ_d is the azimuth angle around \mathbf{h} . Similar to the 4D function in Dynamic NeRF, the spectral BRDF response r can be denoted as:

$$r = f(\theta_h, \theta_d, \varphi_d, \lambda). \quad (2)$$

As shown in Fig. 2, we follow the decomposition in K-Planes [15] to decompose the 4D spectral response into two triplanes. The three planes $\{(\theta_h, \theta_d), (\theta_h, \varphi_d), (\theta_d, \varphi_d)\}$, which depend solely on angular parameters, are designated as the spatial triplane. We denote these three planes as \mathbf{F}_{d1} , \mathbf{F}_{d2} , and \mathbf{F}_{d3} , respectively. Meanwhile, the remaining three planes $\{(\theta_h, \lambda), (\theta_d, \lambda), (\varphi_d, \lambda)\}$ incorporate wavelength dependence and are referred to as the spectral triplane, denoted by \mathbf{F}_{e1} , \mathbf{F}_{e2} , and \mathbf{F}_{e3} . Since the spatial triplane is only related to incident-outgoing angles, it can be shared by both RGB and spectral BRDFs. As discussed in our RGB-spectral joint training strategy, this decomposed representation enables the use of RGB data to enhance spectral BRDF generation.

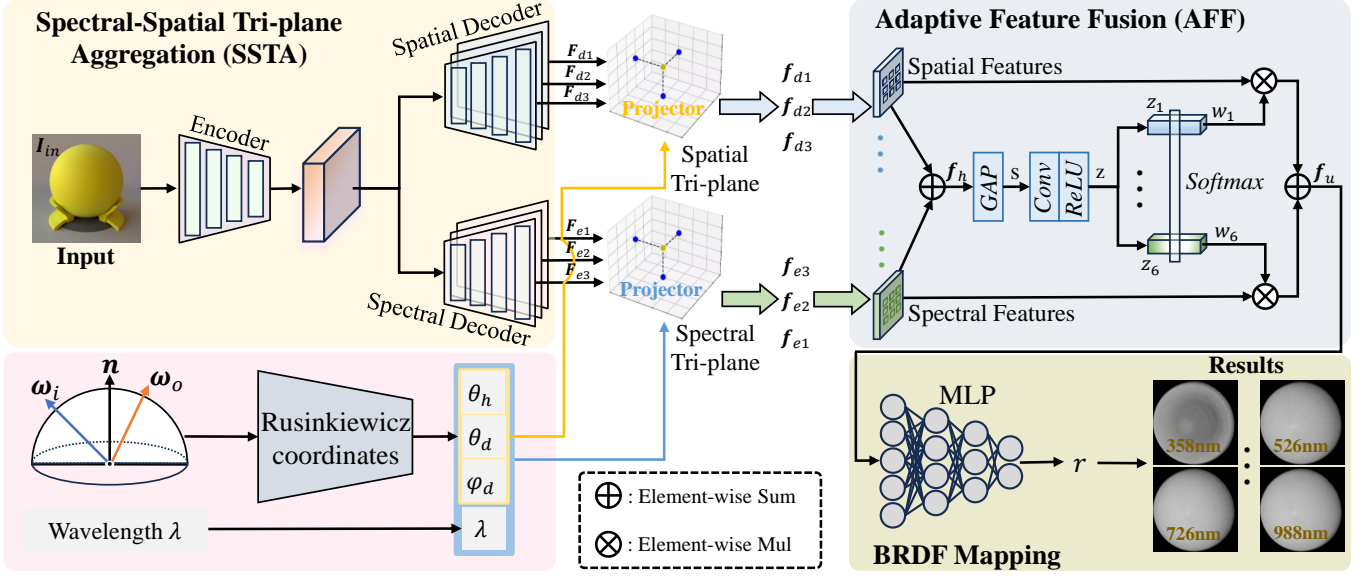


Figure 2: Pipeline of our method.

c) *Image-to-Triplane Mapping*: We employ a CNN-based encoder-decoder network architecture to generate the spatial and spectral triplanes. As shown in Fig. 2, the network input is an RGB image of the target material rendered on a sphere. The output is a 6-channel feature map, which compose the two triplanes: spatial triplane $\{F_{d1}, F_{d2}, F_{d3}\}$ and spectral triplane $\{F_{e1}, F_{e2}, F_{e3}\}$. To obtain the spectral BRDF value, we first calculate the coordinate $(\theta_h, \theta_d, \varphi_d, \lambda)$ and project this coordinate onto the two triplanes, leading to 6 feature vectors with the dimension of C , i.e. ,

$$f_{d1}, f_{d2}, f_{d3} = \left(\mathcal{P}_{F_{d1}}^{(\theta_h, \theta_d)}, \mathcal{P}_{F_{d2}}^{(\theta_h, \varphi_d)}, \mathcal{P}_{F_{d3}}^{(\theta_d, \varphi_d)} \right), \quad (3)$$

$$f_{e1}, f_{e2}, f_{e3} = \left(\mathcal{P}_{F_{e1}}^{(\theta_h, \lambda)}, \mathcal{P}_{F_{e2}}^{(\theta_d, \lambda)}, \mathcal{P}_{F_{e3}}^{(\varphi_d, \lambda)} \right), \quad (4)$$

where \mathcal{P} denotes the projector operator. f_{di} and f_{ei} represent C -dimensional feature vectors associated with the spatial and spectral parameters, respectively. The following section describes how these spatial and spectral features are used to predict the BRDF response.

B. Adaptive Feature Fusion (AFF)

Unlike previous methods [15], [36] that conduct feature fusion via dot product, we propose an Adaptive Feature Fusion (AFF) module, inspired by SKNet [37], to dynamically select appropriate weights for fusing different features. As shown in Fig. 2, we first reshape the C -dimensional 1D feature vectors into 3D feature maps of size $1 \times H \times W$. Then, we apply 3×3 convolutions and element-wise addition to promote feature interaction, resulting in fused hybrid features, denoted as $f_h \in \mathbb{R}^{1 \times H \times W}$:

$$f_h = \sum_{i=1}^3 \text{Conv}(f_{ei}) + \sum_{i=1}^3 \text{Conv}(f_{di}). \quad (5)$$

Next, we perform global average pooling \mathcal{GAP} to obtain the channel statistics s , which capture the global context:

$$s = \mathcal{GAP}(f_h) = \frac{1}{H \times W} \sum_{i=1}^H \sum_{j=1}^W f_h(i, j). \quad (6)$$

To enrich feature representations, inspired by bottleneck structures [38], [39], we first expand s into a descriptor $z \in \mathbb{R}^d$ ($d = 32$) using a 1×1 convolution followed by a ReLU activation. We then apply six parallel, branch-specific convolutions, each with kernel β_i , to reduce the channel dimensionality, enhance inter-channel dependencies, and extract multi-branch feature representations. The process for the i -th branch is as follows:

$$z = \text{ReLU}(\text{Conv}(s)), \quad (7)$$

$$z_i = \text{Conv}(z, \beta_i) \quad \text{for } i = 1, \dots, 6. \quad (8)$$

To adaptively weight different feature branches, we compute an attention score for each branch using a softmax-based mechanism. Specifically, the weight w_i for the i -th branch feature $z_i \in \mathbb{R}$ is obtained as follows:

$$w_i = \text{Softmax}(\text{Reshape}(z_i)). \quad (9)$$

The input spatial and spectral features are re-weighted by their corresponding adaptive scores and then aggregated to form the final fused output $f_u \in \mathbb{R}^C$, which effectively captures the relative importance of different features during fusion:

$$f_u = \text{Reshape} \left(\sum_{i=1}^3 (w_i f_{di} + w_{i+3} f_{ei}) \right). \quad (10)$$

where the reshape operator is used to transform the 2D feature map into a 1D feature vector. With this design, our AFF module effectively enhances feature interaction by adaptively selecting receptive fields for different features and assigning dynamic weights, thus enabling more accurate spectral BRDF reconstruction.

a) *BRDF Mapping Module*: Given the fused feature $\mathbf{f}_u \in \mathbb{R}^C$, we use a three-layer MLP with ReLU activations to decode \mathbf{f}_u and generate the spectral BRDF value r at the coordinate $(\theta_h, \theta_d, \varphi_d, \lambda)$:

$$r = \text{MLP}(\mathbf{f}_u; \delta), \quad (11)$$

where δ are the MLP parameters.

With SSTA feature representation, AFF-based fusion, and this MLP mapping, we predict the spectral reflectance r at each coordinate. Repeating this process over all directions and wavelengths, we reconstruct the full spectral BRDF, enabling flexible spectral image rendering under diverse illumination and geometry.

C. RGB-Spectral Joint Training Strategy

The spatial and spectral decomposition introduced by the SSTA module is designed to address the scarcity of spectral BRDF data in generation tasks by leveraging the abundance of RGB BRDF data. Building on the SSTA module, we propose a joint RGB-spectral training strategy that utilizes both RGB and spectral BRDF data. Below, we detail the workflow and loss functions employed for training on both RGB and spectral BRDF data.

a) *Training on Spectral BRDF*: Measured BRDFs often exhibit a high dynamic range (HDR), resulting in large numerical fluctuations, particularly in the specular components. To address this issue, we apply the μ -law, a logarithmic-relative mapping, to compress the HDR data into a range that is more suitable for training:

$$r' = \frac{\log(1 + \mu |r|)}{\log(1 + \mu)}, \quad (12)$$

where r' denotes the scaled BRDF values, and μ is a compression parameter controlling the degree of compression. In our experiments, we set $\mu = 255$ to achieve effective compression without significantly degrading data quality.

Given N sampled coordinates $(\theta_h, \theta_d, \varphi_d, \lambda)$, we measured the difference between GT and estimated spectral response r'_i and \hat{r}'_i after μ -law, i.e. ,

$$\mathcal{L}_{spec} = \frac{1}{N} \sum_{i=1}^N (\hat{r}'_i - r'_i)^2. \quad (13)$$

Meanwhile, we apply a total variation (TV) loss \mathcal{L}_{TV} to constrain the smoothness of generated spectral BRDF. The total loss on spectral BRDF can be represented as

$$\mathcal{L}_s = \mathcal{L}_{spec} + \alpha \mathcal{L}_{TV}, \quad (14)$$

where coefficient α is set to 2 for balancing the TV loss.

b) *Training on RGB BRDF*: RGB BRDFs and spectral BRDFs share the same spatial tri-plane features (\mathbf{f}_{di}), but differ in their spectral tri-plane features (\mathbf{f}_{ei}). Specifically, for each coordinate $(\theta_h, \theta_d, \varphi_d, \lambda)$ in the spectral BRDF, we sample the corresponding spectral tri-plane feature using the projection operation described in Eq. (4). For the RGB BRDF case, the spectral feature is obtained by averaging all features along the

λ dimension of the spectral triplane at the location $(\theta_h, \theta_d, \varphi_d)$, i.e. ,

$$\hat{\mathbf{f}}_{ei} = \frac{1}{M} \sum_{\lambda} \mathcal{P}_{\mathbf{F}_{ei}}^{(\theta_h, \theta_d, \varphi_d, \lambda)}, \quad (15)$$

where M is the number of sampled wavelengths in the spectral triplane, and $\hat{\mathbf{f}}_{ei}$ denotes the spectral features for the RGB BRDF data. This averaging operation effectively converts the spectral response into a grayscale average reflectance. Given the spatial and spectral features, we predict the response \hat{r}' and supervise it using the grayscale value of the RGB BRDF:

$$\mathcal{L}_{RGB} = \frac{1}{N} \sum_{i=1}^N (\hat{r}' - g')^2, \quad (16)$$

where g' is obtained by averaging the RGB BRDF values across channels and applying the μ -law transformation.

To train SpecGen, we employ the loss functions \mathcal{L}_{RGB} and \mathcal{L}_{spec} for RGB and spectral BRDF data, respectively. This joint training strategy allows us to leverage large-scale RGB BRDF data, significantly enhancing the model's generalization capability.

IV. EXPERIMENT

A. Dataset and Evaluation Metrics

We employ two datasets in our experiments: RGL dataset [6] and MERL dataset [14]. RGL [6] dataset comprises 51 real-world isotropic materials and provides RGB and spectral BRDFs. MERL [14] dataset includes 100 real-world materials. Each material consists of a set of reflectance measurements, parameterized as spherical angles $(\theta_h, \theta_d, \varphi_d)$ derived from the Rusinkiewicz parameterization [35] using the \mathbf{h} and \mathbf{d} vectors. The resolution for each wavelength channel is $90 \times 90 \times 180$, with a total of 1,458,000 reflectance measurements across 195 wavelength channels. Instead of directly comparing tabulated BRDF values, we render the predicted spectral BRDFs on a reference sphere under diverse illumination conditions and compute PSNR [41] and SSIM [41] against images rendered with the GT BRDFs, ensuring that the scores reflect perceptual fidelity in practical use cases.

B. Implementation Details

We implement all experiments using PyTorch with the Adam optimizer [42], setting $\beta_1 = 0.9$ and $\beta_2 = 0.999$. The learning rate is initialized at 1×10^{-4} , batch size is 65,536 (sampled points from multiple materials), and the learning rate decays by half every four epochs for stable convergence. Our model trains for 20 epochs on an RTX 4090 GPU (approx. 20 hours). We use 36 materials from the RGL isotropic dataset [6] for training and 12 for testing. For both, we sample 5,120,000 points per material (about 1/10 of total) and apply μ -law compression to reduce dynamic range. Spectral and spatial triplane dimensions are initialized as [90, 90, 180, 39], with 39 for wavelength channel.

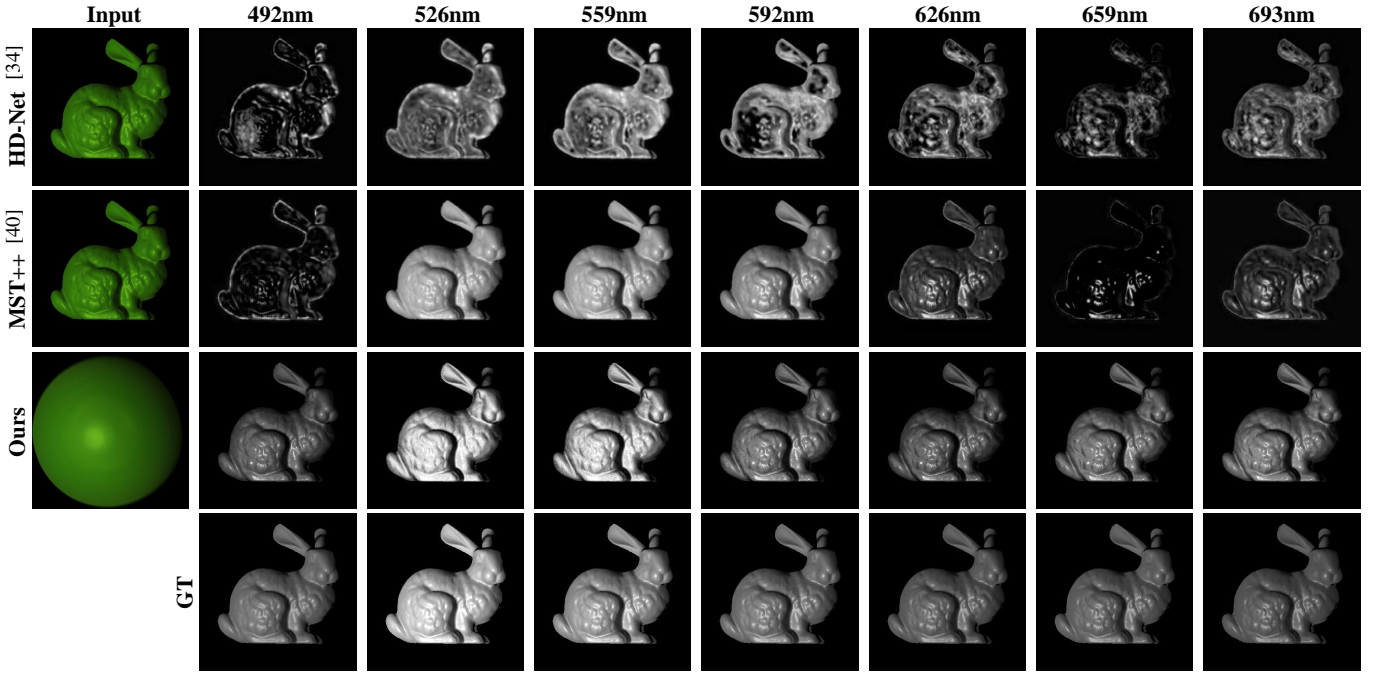


Figure 3: Qualitative comparisons of spectral rendering, where our method takes the RGB sphere input image, generates the spectral BRDF, and renders the spectral bunny image. HSI baselines take the RGB bunny image and directly output the corresponding spectral image.

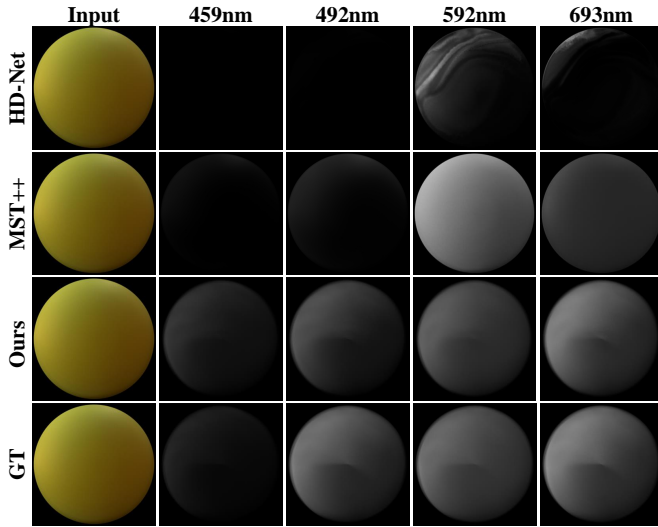


Figure 4: Qualitative comparisons of reconstructed images under environmental illumination are shown alongside results from state-of-the-art hyperspectral image reconstruction methods, including HDNet [40] and MST++ [34]. Our method demonstrates superior spectral accuracy and robustness across different wavelength bands and lighting conditions, yielding reconstructed images that closely match the GT and outperform existing approaches in visual fidelity.

C. Evaluation on Spectral BRDF Generation

a) Baselines: Our method effectively reconstructs spectral BRDFs of various materials from just a single input image, enabling detailed rendering of spectral images at different

Table II: Quantitative comparisons on spectral rendering between our method and existing hyperspectral image reconstruction methods under environmental lights (**top**) and distant lights (**middle**).

Material	HD-Net [40]		MST++ [34]		Ours	
	PSNR↑	SSIM↑	PSNR↑	SSIM↑	PSNR↑	SSIM↑
acrylic-felt-yellow	18.64	0.6737	20.85	0.7103	29.39	0.9303
ilm-13-37-dark-green	31.32	0.7912	28.27	0.7448	47.36	0.9677
cc-ibiza-sunset	24.94	0.6690	26.63	0.7010	38.19	0.8951
acrylic-felt-yellow	25.01	0.5989	29.12	0.7476	29.47	0.8292
ilm-13-37-dark-green	33.03	0.9852	32.51	0.9514	39.57	0.9671
cc-ibiza-sunset	25.53	0.9627	24.77	0.9491	27.34	0.9155
Average	26.41	0.7801	27.03	0.8007	35.22	0.9175

wavelengths for diverse purposes. In contrast, hyperspectral image reconstruction methods directly recover spectral images from input images with a different focus. Although their objectives differ, both produce spectral representations evaluable for fidelity and overall accuracy. Thus, we assess our model’s performance by comparing the quality of rendered spectral images using well-established metrics like PSNR [41] and SSIM [41] under controlled experimental conditions. We compare with state-of-the-art hyperspectral methods, including HD-Net [40], for high-resolution recovery, and MST++ [34], using a mask-guided transformer for spectral reconstruction.

b) Qualitative and Quantitative Assessment: As shown in Table II, for three representative materials, we input images of spheres rendered under both environmental and distant lights and use our method alongside baseline models to render spectral images at nine uniformly selected wavelengths for quantitative comparison. The results demonstrate that

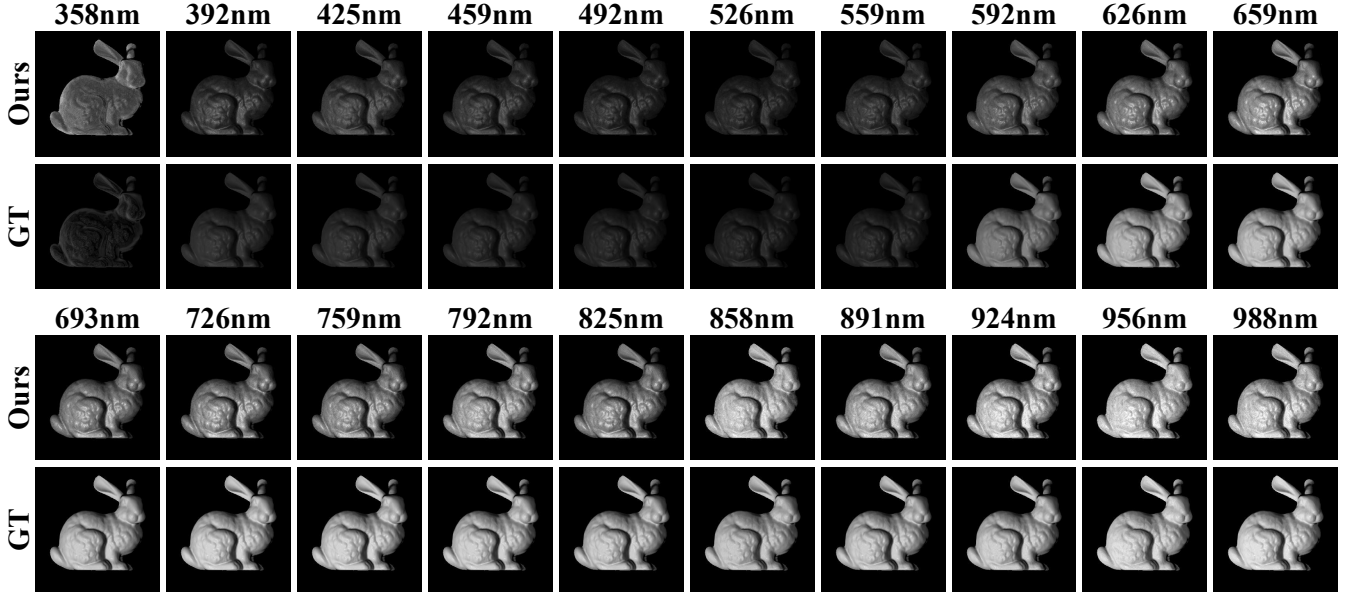


Figure 5: Rendered images of the same material across additional wavelengths (400–1000 nm), using the same input as in Fig. 1. Comparison with the GT further demonstrates the accuracy of our method.

Table III: Ablation studies on the robustness of our method under different environmental lights. Gray cells indicate environmental lights present in training datasets. Our method shows generalization even in environmental light that is not covered by the training dataset.

Env. Light	acrylic-felt-yellow		ilm-l3-37-matte	
	PSNR↑	SSIM↑	PSNR↑	SSIM↑
Outdoor Env. map	39.44	0.9609	41.95	0.9847
Indoor Env. map1	38.28	0.9551	41.06	0.9781
Indoor Env. map2	36.72	0.9705	40.39	0.9812
Average	38.15	0.9622	41.13	0.9813

our method surpasses the baselines in multispectral image reconstruction under varying lighting conditions, achieving an average PSNR improvement of over 8 dB. Furthermore, as shown in Fig. 3, our method consistently produces spectral reconstructions that are much closer to the GT than HSI reconstruction methods, not only under parallel lighting but also across a wide range of environmental illumination conditions and spectral bands. Additional qualitative results in Fig. 4 further demonstrate the superior generalization and robustness of our approach in challenging environment light scenarios, with accurate rendering across the visible and near-infrared spectra.

In addition, while existing HSI methods are typically constrained to the 400–700 nm wavelength range and can only generate hyperspectral images of the same shape, our method enables spectral rendering over a broader wavelength spectrum and produces spectral BRDFs for multispectral rendering of different objects. Fig. 5 presents additional results of spectral renderings for various materials at representative wavelengths

Table IV: Evaluation on the effectiveness of boosting spectral BRDF generation via RGB BRDF data on 12 test spectral BRDF data. We calculate PSNR and SSIM of spectral rendering of a sphere using GT and generated spectral BRDFs under distant light.

Material	RGL-S		RGL-C-S+MERL	
	PSNR↑	SSIM↑	PSNR↑	SSIM↑
acrylic-felt-green	33.28	0.8651	34.50	0.8793
acrylic-felt-orange	33.73	0.9292	32.46	0.8770
acrylic-felt-purple	31.21	0.7196	31.87	0.8135
acrylic-felt-yellow	30.70	0.9104	28.08	0.8638
leaf-maple	34.67	0.7621	33.62	0.7484
ilm-l3-37-matte	29.70	0.8740	28.56	0.8881
cc-ibiza-sunset	28.98	0.7976	31.81	0.9354
ilm-l3-37-metallic	25.37	0.5473	27.02	0.8147
colodur-kalahari-2a	28.43	0.9157	29.07	0.8761
chm-light-blue	31.29	0.8416	32.61	0.8490
spectralon	25.38	0.8983	27.80	0.8420
colodur-napoli-4f	36.48	0.8881	42.35	0.9622
Average	30.77	0.8291	31.65	0.8625

spanning the visible and near-infrared regions, demonstrating the generalization ability and high fidelity of our approach across a wider spectral range. Moreover, as shown in Fig. 3, after deriving the spectral BRDF from the input sphere image, our method can render the multispectral image of the bunny shape, achieving better reconstruction results over a broad wavelength range.

c) Robustness Assessment: In real-world scenarios, materials are often illuminated under varying environmental lighting conditions. A robust reconstruction method should maintain high recovery fidelity regardless of these variations.

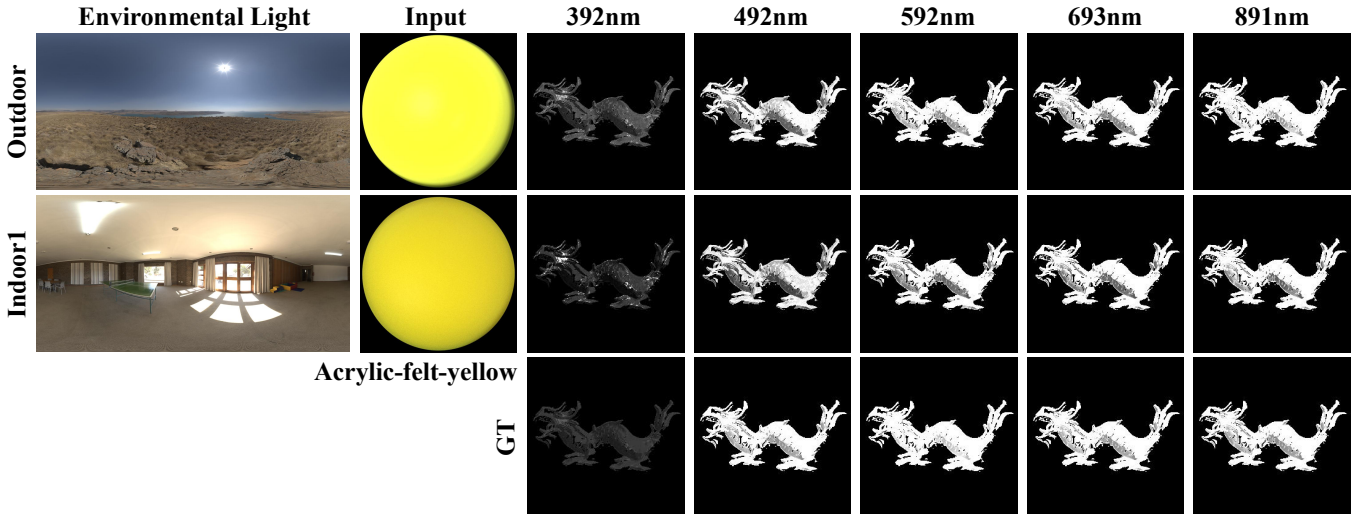


Figure 6: Spectral BRDF results for “acrylic-felt-yellow” generated from inputs rendered under diverse unseen environmental lights (Outdoor, Indoor1), with outputs rendered under distant light. The left side displays the environmental lights used for rendering the input images. Our method demonstrates robust performance across varying environmental lighting conditions, closely matching the GT across wavelengths.

Table V: Ablation studies on triplane feature fusion modules, including Hadamard product used in K-Planes [15] and our proposed AFF module.

Method	RGL-S		RGL-C-S+MERL	
	PSNR↑	SSIM↑	PSNR↑	SSIM↑
Hadamard [15]	27.00	0.7837	26.83	0.8159
AFF (Ours)	30.77	0.8291	31.65	0.8625

As shown in Table III, we evaluate our model using three different environmental lighting setups: Outdoor Env. map, Indoor Env. map1, and Indoor Env. map2. Notably, Indoor Env. map2 was included in the training datasets, while the other two were unseen during training. We rendered reconstructed images at 20 different wavelengths, computing PSNR and SSIM as the average across these wavelengths to assess reconstruction quality. The result that our method still performs well under previously unseen illumination shows that our model exhibits strong robustness to different environmental lighting. Additionally, as illustrated in Fig. 6, qualitative visualizations confirm this robustness in the same material, with our method producing realistic and highly accurate renderings across different wavelengths, closely matching the GT.

D. Ablation study

a) Training strategy: To evaluate the effectiveness of our RGB-spectral joint training strategy in addressing the data scarcity problem, we conduct ablation studies comparing our method with and without the inclusion of RGB BRDF data during training. Specifically, we define two training sets: (1) RGL-S, which contains 36 spectral BRDFs from the RGL dataset [6]; and (2) RGL-C-S+MERL, which comprises RGL-S, 51 additional RGB BRDFs (RGL-C) from the RGL dataset [6], and an extra 100 RGB BRDFs from the MERL dataset [14].

We train SpecGen on these two datasets and evaluate the model on 12 unseen spectral BRDFs. As shown in Table IV, integrating RGB data into the training set significantly improves spectral reconstruction accuracy, yielding an average PSNR improvement of nearly 0.9 dB compared to using only spectral data.

Furthermore, we provide a qualitative comparison in Fig. 7, showcasing results across seven different wavelengths for two materials. The qualitative results demonstrate that incorporating RGB data into training enables our proposed model to predict reflectance more accurately across various wavelengths, producing rendered images that closely match the GT. This experiment result efficiently highlights the effectiveness of leveraging RGB-BRDF data to enhance spectral BRDF reconstruction, further demonstrating the rationalization of our training strategy.

b) Adaptive Feature Fusion Module: Previous studies [15] have highlighted the effectiveness of the Hadamard product in triplane feature fusion. To evaluate whether our proposed Adaptive Feature Fusion (AFF) module offers a more efficient alternative, we conduct a correlation ablation study in Table V. The ablation results demonstrate a significant advantage of our AFF in multiplanar feature fusion, achieving an average PSNR improvement of 4.3 dB across two test datasets compared to the Hadamard product strategy, showing the rationality and strength of the adaptive selection fusion mechanism in our AFF module.

V. CONCLUSION

We propose SpecGen, the first framework for generating spectral BRDFs from a single RGB image of a sphere, enabling photorealistic spectral rendering under arbitrary illuminations and geometries. Our method addresses the fundamental challenge of spectral BRDF data scarcity by using abundant RGB BRDF data to enhance spectral BRDF generation, which is achieved by our Spectral-Spatial Tri-plane Aggregation

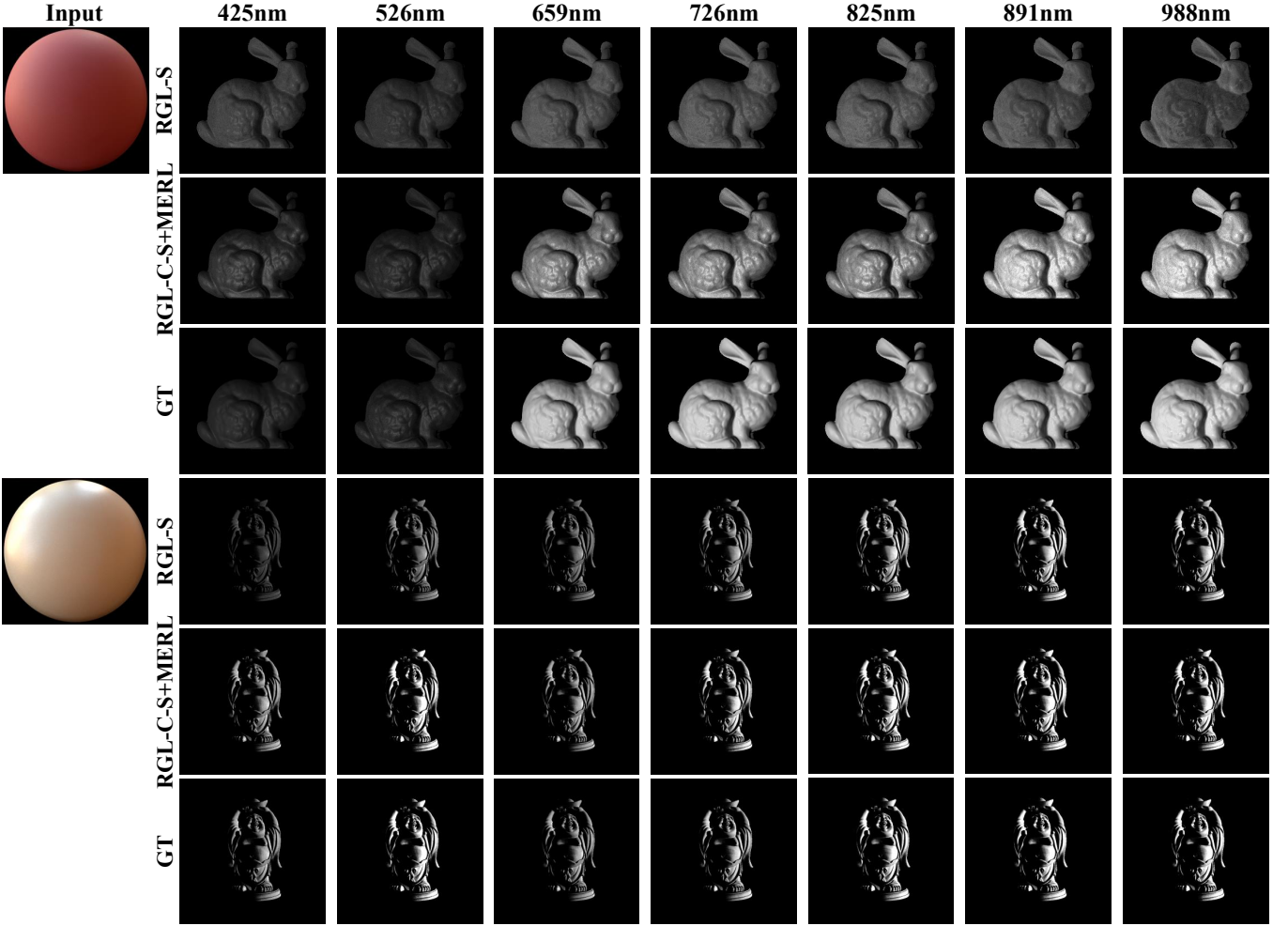


Figure 7: Qualitative comparisons of rendering results using only spectral BRDF dataset RGL-S vs. spectral plus RGB BRDF dataset RGL-C-S+MERL, where top and bottom parts denote two different test materials. With the help of our training strategy building upon our SSTA network, we can leverage RGB BRDF data to boost the spectral rendering quality.

(SSTA) network that decouples reflectance modeling into spectral and spatial domains. Furthermore, our Adaptive Feature Fusion (AFF) module effectively integrates multi-plane features, overcoming the limitations of fixed fusion operators. Extensive experiments show the performance of our SpecGen on publicly available spectral BRDF datasets and downstream spectral rendering tasks.

VI. LIMITATIONS AND FUTURE WORK

Although the proposed SpecGen framework delivers encouraging results, there are a few aspects that could benefit from additional investigation.

a) Limitations: First, since the sampling patterns used during training do not fully match the illumination distributions at test time, renderings under complex environment maps occasionally exhibit mild artifacts, as shown in Fig. 4. Existing neural sampling techniques developed for RGB BRDFs provide valuable insights, yet the higher dimensionality of spectral BRDFs means that these RGB-oriented strategies do not always carry over directly. Second, even with the aid of a total-variation term that promotes smoothness, faint noise can still appear

on highly continuous surfaces (e.g., spheres). We attribute this mainly to the present tri-plane formulation, which may be less expressive for extremely smooth functions. Third, the current prototype is tailored to a single RGB photograph; this design choice simplifies network conditioning but also restricts immediate applicability to scenes that feature more complex geometry or spatially varying materials.

b) Future Work: We plan to extend SpecGen toward scene-level spectral BRDF estimation so that spatially varying materials in real-world environments can be reconstructed from casual multi-view imagery. Another promising direction is the development of neural sampling schemes specifically tuned to the spectral domain, which may better accommodate its higher dimensional characteristics. We are also interested in incorporating adaptive wavelength discretization strategies to cover broader spectral ranges and to model anisotropic reflectance effects. Finally, we will explore additional regularization techniques, more flexible multi-plane decompositions, and lightweight model variants to reduce memory footprint and inference time while further suppressing residual noise and improving output smoothness.

REFERENCES

- [1] H. Ghassemian, “A review of remote sensing image fusion methods,” *Information Fusion*, vol. 32, pp. 75–89, 2016.
- [2] X. Cheng, X. He, M. Qiao, P. Li, P. Chang, T. Zhang, X. Guo, J. Wang, Z. Tian, and G. Zhou, “Multi-view graph convolutional network with spectral component decompose for remote sensing images classification,” *IEEE Transactions on Circuits and Systems for Video Technology*, vol. 35, no. 1, pp. 3–18, 2022.
- [3] K. Choudhary, B. DeCost, C. Chen, A. Jain, F. Tavazza, R. Cohn, C. W. Park, A. Choudhary, A. Agrawal, S. J. Billinge *et al.*, “Recent advances and applications of deep learning methods in materials science,” *npj Computational Materials*, vol. 8, no. 1, p. 59, 2022.
- [4] T. Kang, M. Chae, E. Seo, M. Kim, and J. Kim, “Deephandsvr: Hand interface using deep learning in immersive virtual reality,” *Electronics*, vol. 9, no. 11, p. 1863, 2020.
- [5] K. Ding, T. Lu, W. Fu, and L. Fang, “Cross-scene hyperspectral image classification with consistency-aware customized learning,” *IEEE Transactions on Circuits and Systems for Video Technology*, 2024.
- [6] J. Dupuy and W. Jakob, “An adaptive parameterization for efficient material acquisition and rendering,” *ACM Transactions on graphics (ToG)*, vol. 37, no. 6, pp. 1–14, 2018.
- [7] F. Gokbudak, A. Sztrajman, C. Zhou, F. Zhong, R. Mantiuk, and C. Oztireli, “Hypernetworks for generalizable brdf representation,” in *ECCV*. Springer, 2025, pp. 73–89.
- [8] G. Vecchio, R. Martin, A. Roullier, A. Kaiser, R. Rouffet, V. Deschaintre, and T. Boubekeur, “Controlmat: a controlled generative approach to material capture,” *ACM Transactions on Graphics (ToG)*, vol. 43, no. 5, pp. 1–17, 2024.
- [9] G. Vecchio, R. Sortino, S. Palazzo, and C. Spampinato, “Matfuse: controllable material generation with diffusion models,” in *CVPR*, 2024, pp. 4429–4438.
- [10] Y. Li, W. Xie, and H. Li, “Hyperspectral image reconstruction by deep convolutional neural network for classification,” *Pattern Recognition*, vol. 63, pp. 371–383, 2017.
- [11] L. Wang, C. Sun, Y. Fu, M. H. Kim, and H. Huang, “Hyperspectral image reconstruction using a deep spatial-spectral prior,” in *CVPR*, June 2019.
- [12] P. Liu, Y. Zhao, K. Feng, and S. G. Kong, “Physics-driven multispectral filter array pattern optimization and hyperspectral image reconstruction,” *IEEE Transactions on Circuits and Systems for Video Technology*, vol. 34, no. 10, pp. 9528–9539, 2024.
- [13] H. Chen, W. Zhao, T. Xu, G. Shi, S. Zhou, P. Liu, and J. Li, “Spectral-wise implicit neural representation for hyperspectral image reconstruction,” *IEEE Transactions on Circuits and Systems for Video Technology*, vol. 34, no. 5, pp. 3714–3727, 2023.
- [14] W. Matusik, “A data-driven reflectance model,” Ph.D. dissertation, Massachusetts Institute of Technology, 2003.
- [15] S. Fridovich-Keil, G. Meanti, F. R. Warburg, B. Recht, and A. Kanazawa, “K-planes: Explicit radiance fields in space, time, and appearance,” in *CVPR*, 2023, pp. 12 479–12 488.
- [16] V. Deschaintre, G. Drettakis, and A. Bousseau, “Guided fine-tuning for large-scale material transfer,” in *Computer Graphics Forum*, vol. 39, no. 4. Wiley Online Library, 2020, pp. 91–105.
- [17] X. Li, Y. Dong, P. Peers, and X. Tong, “Modeling surface appearance from a single photograph using self-augmented convolutional neural networks,” *ACM Transactions on Graphics (ToG)*, vol. 36, no. 4, pp. 1–11, 2017.
- [18] V. Deschaintre, M. Aittala, F. Durand, G. Drettakis, and A. Bousseau, “Flexible svbrdf capture with a multi-image deep network,” in *Computer graphics forum*, vol. 38, no. 4. Wiley Online Library, 2019, pp. 1–13.
- [19] —, “Single-image svbrdf capture with a rendering-aware deep network,” *ACM Transactions on Graphics (ToG)*, vol. 37, no. 4, pp. 1–15, 2018.
- [20] G. Vecchio, S. Palazzo, and C. Spampinato, “Surfacenet: Adversarial svbrdf estimation from a single image,” in *ICCV*, 2021, pp. 12 840–12 848.
- [21] Y. Guo, C. Smith, M. Hašan, K. Sunkavalli, and S. Zhao, “Materialgan: Reflectance capture using a generative svbrdf model,” *arXiv preprint arXiv:2010.00114*, 2020.
- [22] X. Zhou, M. Hasan, V. Deschaintre, P. Guerrero, K. Sunkavalli, and N. K. Kalantari, “Tilegen: Tileable, controllable material generation and capture,” in *SIGGRAPH Asia*, 2022, pp. 1–9.
- [23] X. Zhou, M. Hasan, V. Deschaintre, P. Guerrero, Y. Hold-Geoffroy, K. Sunkavalli, and N. K. Kalantari, “Photomat: A material generator learned from single flash photos,” in *SIGGRAPH*, 2023, pp. 1–11.
- [24] J. Ho, A. Jain, and P. Abbeel, “Denoising diffusion probabilistic models,” in *NeurIPS*, vol. 33, 2020, pp. 6840–6851.
- [25] M. Fischer and T. Ritschel, “Metappearance: Meta-learning for visual appearance reproduction,” *ACM Transactions on Graphics (ToG)*, vol. 41, no. 6, pp. 1–13, 2022.
- [26] X. Zhou and N. K. Kalantari, “Look-ahead training with learned reflectance loss for single-image svbrdf estimation,” *ACM Transactions on Graphics (ToG)*, vol. 41, no. 6, pp. 1–12, 2022.
- [27] B. Burley and W. D. A. Studios, “Physically-based shading at disney,” in *SIGGRAPH*, vol. 2012, no. 2012. vol. 2012, 2012, pp. 1–7.
- [28] T. Narumoto, H. Santo, and F. Okura, “Synthesizing time-varying brdfs via latent space,” in *ECCV*. Springer, 2024, pp. 109–124.
- [29] R. Hanocka, A. Hertz, N. Fish, R. Giryes, S. Fleishman, and D. Cohen-Or, “Meshcnn: a network with an edge,” *ACM Transactions on Graphics (ToG)*, vol. 38, no. 4, pp. 1–12, 2019.
- [30] V. Sitzmann, J. Martel, A. Bergman, D. Lindell, and G. Wetzstein, “Implicit neural representations with periodic activation functions,” in *NeurIPS*, vol. 33, 2020, pp. 7462–7473.
- [31] B. Mildenhall, P. P. Srinivasan, M. Tancik, J. T. Barron, R. Ramamoorthi, and R. Ng, “Nerf: Representing scenes as neural radiance fields for view synthesis,” *Communications of the ACM*, vol. 65, no. 1, pp. 99–106, 2021.
- [32] A. Simeonov, Y. Du, A. Tagliasacchi, J. B. Tenenbaum, A. Rodriguez, P. Agrawal, and V. Sitzmann, “Neural descriptor fields: Se (3)-equivariant object representations for manipulation,” in *ICRA*. IEEE, 2022, pp. 6394–6400.
- [33] Y. Chen, G. Jia, Y. Zha, P. Zhang, and Y. Zhang, “Linr: A plug-and-play local implicit neural representation module for visual object tracking,” *IEEE Transactions on Circuits and Systems for Video Technology*, 2025.
- [34] Y. Cai, J. Lin, X. Hu, H. Wang, X. Yuan, Y. Zhang, R. Timofte, and L. Van Gool, “Mask-guided spectral-wise transformer for efficient hyperspectral image reconstruction,” in *CVPR*, 2022, pp. 17 502–17 511.
- [35] S. M. Rusinkiewicz, “A new change of variables for efficient brdf representation,” in *Rendering Techniques’ 98: Proceedings of the Eurographics Workshop in Vienna, Austria, June 29–July 1, 1998*. Springer, 1998, pp. 11–22.
- [36] W. Li, H. Guo, Y. Hou, G. Gao, and Z. Ma, “Dual-domain modulation network for lightweight image super-resolution,” *IEEE Transactions on Multimedia*, 2025.
- [37] X. Li, W. Wang, X. Hu, and J. Yang, “Selective kernel networks,” in *CVPR*, 2019, pp. 510–519.
- [38] J. Hu, L. Shen, and G. Sun, “Squeeze-and-excitation networks,” in *CVPR*, 2018, pp. 7132–7141.
- [39] W. Li, H. Guo, X. Liu, K. Liang, J. Hu, Z. Ma, and J. Guo, “Efficient face super-resolution via wavelet-based feature enhancement network,” in *ACM MM*, 2024, pp. 4515–4523.
- [40] X. Hu, Y. Cai, J. Lin, H. Wang, X. Yuan, Y. Zhang, R. Timofte, and L. Van Gool, “Hdnet: High-resolution dual-domain learning for spectral compressive imaging,” in *CVPR*, 2022, pp. 17 542–17 551.
- [41] Z. Wang and A. C. Bovik, “A universal image quality index,” *IEEE Signal Processing Letters*, vol. 9, no. 3, pp. 81–84, 2002.
- [42] D. P. Kingma and J. Ba, “Adam: A method for stochastic optimization,” *arXiv preprint arXiv:1412.6980*, 2014.